



# Heterogeneous tantalum photonic integrated circuits for sub-micron wavelength applications

NIMA NADER,<sup>1,\*</sup>  ERIC J. STANTON,<sup>1,2,3</sup>  GRANT M. BRODNIK,<sup>2,4</sup>  NUSRAT JAHAN,<sup>1,2</sup> SKYLER C. WEIGHT,<sup>1,2</sup> LINDELL M. WILLIAMS,<sup>2,4</sup> ALI ESHAGHIAN DORCHE,<sup>1,2,5</sup>  KEVIN L. SILVERMAN,<sup>1</sup> SAE WOO NAM,<sup>1</sup> SCOTT B. PAPP,<sup>4</sup>  AND RICHARD P. MIRIN<sup>1</sup> 

<sup>1</sup>Applied Physics Division, National Institute of Standards and Technology, 325 Broadway, Boulder, Colorado 80305, USA

<sup>2</sup>Department of Physics, University of Colorado, 2000 Colorado Avenue, Boulder, Colorado 80309, USA

<sup>3</sup>Currently with EMode Photonix, Boulder, Colorado 80305, USA

<sup>4</sup>Time and Frequency Division, National Institute of Standards and Technology, 325 Broadway, Boulder, Colorado 80305, USA

<sup>5</sup>Currently with Nexus Photonics, 6500 Hollister Avenue, Suite 150, Goleta, California 93117, USA

\*nima.nader@nist.gov

Received 6 January 2025; revised 23 March 2025; accepted 1 April 2025; published 24 April 2025

Atomic and trapped-ion systems are the backbone of an emerging generation of quantum-based positioning, navigation, and timing (PNT) technologies. The miniaturization of such quantum systems offers tremendous technological advantages, especially the reduction of system size, weight, and power consumption. Yet this has been limited by the absence of compact, standalone photonic integrated circuits (PICs) at the wavelengths suitable for these instruments. Mobilizing such photonic systems requires the development of fully integrated, on-chip, active components at sub-micrometer wavelengths. We demonstrate heterogeneous photonic integrated circuits operating at 980 nm based on wafer-scale bonding of InGaAs quantum well active regions to tantalum pentoxide passive components. This high-yield process provides >95% surface area yield and enables integration of >1300 active components on a 76.2 mm (3 inch) silicon wafer. We present a diverse set of functions, including semiconductor optical amplifiers, Fabry–Pérot lasers, and distributed feedback lasers with a 43 dB side-mode suppression ratio and a >250 GHz single-mode tuning range. We test the precise wavelength control and system-level functionality of the on-chip lasers by pumping optical parametric oscillation processes in microring resonators fabricated on the same platform, generating short-wavelength signals at 778 nm and 752 nm. These results provide a pathway to realize fully functional integrated photonic engines for the operation of compact quantum sensors based on atomic and trapped-ion systems. © 2025 Optica Publishing Group under the terms of the

Optica Open Access Publishing Agreement

<https://doi.org/10.1364/OPTICA.554862>

## 1. INTRODUCTION

Quantum systems based on optically controlled neutral atoms and trapped ions are a critical component of several emerging technologies. These include quantum information processing with trapped-ion qubits [1,2], optical atomic clocks [3–5], cold-atom interferometers [6–8] for Global Positioning System (GPS)-free navigation, magnetometers [9,10], and gravimeters [11]. Given the broad application base, a significant effort has been placed on developing such systems with a reduced form factor through microfabrication of small-scale vapor cells [12,13] and ion traps [14] and integration with photonic circuits [15–20]. Despite this progress, quantum systems have not reached their full scalability and miniaturization potential. This is partly due to the limited access to on-chip laser sources and heterogeneous photonic integrated circuits (PICs) at the required wavelengths for the control of such systems, including visible and ultraviolet wavelengths [3,4,21–26].

The demand from datacom and telecom industries has resulted in the rapid development of heterogeneous PICs at wavelengths around 1310 and 1550 nm [27–30]. These platforms are based on the integration of InAs quantum dot [31] and InP-based quantum well (QW) [32] gain regions with silicon-on-insulator photonics. Such platforms do not support sub-micrometer wavelengths due to the type of gain media and the silicon bandgap absorption. The inability to use silicon photonics at these shorter wavelengths necessitates the development of platforms involving large bandgap and low refractive index photonic materials. Recently, short-wavelength heterogeneous PICs have been demonstrated based on chip-scale bonding of GaAs-based actives on silicon nitride (Si<sub>3</sub>N<sub>4</sub>) with system functionality at 980 [33] and 780 nm [34]. Heterogeneous integration with large band-gap crystalline thin-film lithium niobate (TFLN) has also been explored [35]. This would be a promising platform if GaAs-to-TFLN optical coupling structures are developed for full system integration between active and passive components.

In this paper, we present a new integrated photonic platform based on heterogeneous integration of InGaAs-on-GaAs QW active regions and tantalum pentoxide ( $\text{Ta}_2\text{O}_5$ , also known as tantala) passive regions. Tantala is an ultra-low-loss, large band-gap, deposited dielectric with a refractive index of  $\approx 2.11$  at 980 nm [36]. Tantala offers key material properties and processing advantages that make it an appealing photonic platform for wafer-scale integration with active components. It benefits from a wide transparency window spanning from the ultraviolet to the mid-infrared, has a small thermo-optic coefficient ( $8.8 \times 10^{-6}$  1/K, [37]), and a large third-order nonlinear coefficient ( $6.2 \times 10^{-19}$  m<sup>2</sup>/W, [37]). In terms of processing, tantala can be deposited at room temperature using ion-beam sputtering with low residual stress and ultra-low thickness nonuniformity of  $\pm 2\%$ , requires a much lower (compared to  $\text{Si}_3\text{N}_4$ ) annealing temperature of  $< 500^\circ\text{C}$  to achieve low material absorption, and can be etched using standard fluorine-chemistry-based dry etch processes (as opposed to the challenging dry etching of TFLN). This III–V semiconductor/tantala platform offers sub-micrometer functionality at 980 nm with various components, such as semiconductor optical amplifiers (SOAs), Fabry–Pérot (FP) lasers, and tunable, single-mode distributed feedback (DFB) lasers. We further show the utility of the single-mode lasers by pumping wide-span degenerate optical parametric oscillation (OPO) processes based on the third-order,  $\chi^{(3)}$ , nonlinearity [38] in dispersion-engineered microring resonators.

## 2. WAFER-SCALE FABRICATION

Heterogeneous PICs consist of III–V epitaxial layer stacks integrated with passive photonics on a common substrate. Fabrication processes developed for such integration are predominantly based on chiplet-level integration methods, such as microtransfer printing [39] and chip-scale bonding [33]. In microtransfer printing, the active devices are formed on their native substrate (InP or GaAs) and then released and transferred to the Si-based photonic circuit using a polydimethylsiloxane (PDMS) stamp [39]. This method simplifies the processing by enabling the fabrication of active components on their native substrate but requires the design of misalignment-tolerant structures due to its coarse alignment accuracy of  $\pm 500$  nm [39,40]. In the case of chip-scale bonding, it enables the co-fabrication of passive photonics and active components with precise alignment limited by the lithography step. This process also enables the bonding of III–V materials with different designs on the same photonic wafer. The final device yield is, however, limited by the number of bonded III–V chips and their surface area [41].

We develop a fabrication process based on 76.2 mm (3 in.) wafer-scale bonding of a III–V semiconductor layer stack to a silicon wafer with tantala PICs. The wafer-scale bonding process enables utilization of the entire wafer, with  $> 95\%$  surface area yield, to achieve dense integration of active and passive components with  $< 10$  nm alignment accuracy (limited by lithography instrumentation). We utilize this process to yield  $> 40$  chips with more than a 1000 integrated active components. Figure 1(a) presents the simplified wafer-scale process flow. We grow the AlGaAs/InGaAs active layers lattice-matched to a 76.2 mm GaAs substrate using molecular beam epitaxy. The epitaxial layer stack consists of two 7.25 nm thick  $\text{In}_{21}\text{Ga}_{79}\text{As}$  QW layers separated by 10 nm thick GaAs barriers [42,43] (see Supplement 1 for the full epitaxial layer stack). A 570 nm thick tantala film is ion-beam

sputtered on an oxidized Si wafer with 800 nm thick thermal  $\text{SiO}_2$  to form the waveguiding layer of the PIC. The waveguide structures, including the routing waveguides, chip couplers, and feedback structures required for the operation of integrated lasers, are formed by electron beam lithography (EBL) and dry etch processes based on  $\text{CHF}_3/\text{CF}_4/\text{Ar}$  plasma. The 76.2 mm GaAs epi-wafer is then directly bonded to the tantala wafer after using atomic layer deposition (ALD) to deposit 12 nm of an  $\text{Al}_2\text{O}_3$  interlayer and  $\text{O}_2$  plasma surface activation. After bonding, the GaAs substrate is removed with a  $\text{NH}_4\text{OH}/\text{H}_2\text{O}_2$  wet etch process to expose the epitaxial semiconductor layer stack (refer to Fig. 2S of Supplement 1 for a camera image of the wafer-scale bonded epitaxy on the tantala wafer).

To form the electrically pumped active components [Fig. 1(e)], we first form contacts to the *p*-type Be-doped GaAs layer on top of the III–V layer stack through lift-off of a deposited Ti/Au/Ti (5 nm/50 nm/5 nm) film. Next, the laser mesa and the bottom *n*-contact structures are EBL patterned and dry-etched by a  $\text{BCl}_3/\text{Cl}_2/\text{Ar}$  chemistry. Following the III–V etch, 10 nm ALD  $\text{Al}_2\text{O}_3$  is deposited to passivate the etched sidewalls of the III–V structure, and electrical contact to the *n*-type Si-doped semiconductor is formed by lift-off of a 50/100/250/5 nm thick Pd/Ge/Au/Ti metal stack. We then deposit a 1.4  $\mu\text{m}$  thick layer of  $\text{SiO}_2$  as optical top-cladding for the tantala waveguides and electrical isolation for the diodes. Figure 1(b) presents a camera picture of the processed 76.2 mm wafer after the  $\text{SiO}_2$  top-cladding deposition. Fabrication of the lasers is completed via etching into the top-cladding to access the contact metals and electron beam deposition of 1  $\mu\text{m}$  thick gold probe pads [Figs. 1(c) and 1(d)].

A crucial component enabling heterogeneous PICs is a coupling structure that facilitates efficient light coupling from the III–V material to passive waveguides. Achieving an efficient mode transition from the high refractive index III–V device ( $n_{\text{eff}} \approx 3.32$ ) to the low index tantala waveguide ( $n_{\text{eff}} \approx 1.95$ ) requires the design of complex photonic structures. One possible design is based on the use of an intermediary material as a mode converter [33]. In our design, the coupling structure is based on multistage inverse tapers etched at the two ends of the III–V active region [Fig. 1(f)]. The high refractive index of the III–V results in an optical mode that is mostly localized in the III–V mesa. We first taper the III–V ridge from the primary active region width to a 100 nm tip [red-colored taper in Fig. 1(f)]. This reduces the effective modal index such that it enables efficient optical mode transition to the underlying *n*-contact layer. The *n*-contact layer [orange-colored area in Fig. 1(f)] is then tapered to a 100 nm tip in two stages to facilitate light coupling to the tantala waveguide with a simulated 86% efficiency (the details of the multistage taper design are provided in Supplement 1).

## 3. INTEGRATED SINGLE-MODE LASERS

Single-mode lasers will be at the heart of integrated photonic engines designed for the control and operation of compact atomic systems [33,34,44]. Distributed feedback (DFB) lasers are one of the most widely used single-mode lasers due to their simple cavity design, high side-mode suppression ratio (SMSR), and long-term stability. A free-running DFB laser, however, exhibits a typical linewidth of a few megahertz, which is broader than required for many applications in quantum science and technology. Recently, it has been demonstrated that the frequency noise of these lasers can be suppressed by  $> 20$  dB [45,46] to outperform stabilized

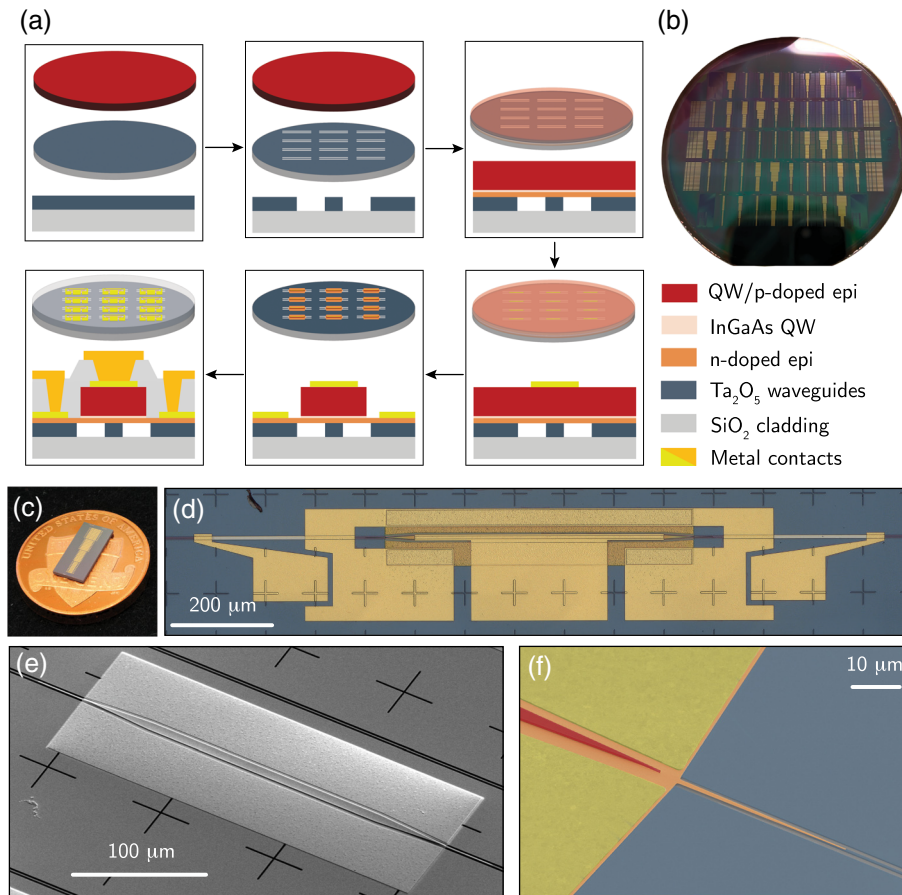


**Fig. 1.** Wafer-scale fabrication of heterogeneous tantalum PICs. (a) Simplified process flow depicting the wafer-scale bonding of the III–V material stack and formation of the active components. (b) Camera image of the fabricated 76.2 mm wafer after SiO<sub>2</sub> top-cladding deposition. (c) Focus-stacked camera image of a fully functional chip with 32 integrated active components. (d) Microscope image of an on-chip DFB laser. (e) Scanning electron micrograph (SEM) of a patterned and etched III–V active region integrated on tantalum waveguides. (f) Zoomed-in, false color, and SEM of the III–V to tantalum transition taper structure. Here, the colors match the color scheme in (a).

fiber laser sources [47] when they are self-injection locked to high-quality factor, low-mode-volume microresonators in low-loss PICs.

We fabricate and characterize DFB lasers on the III–V/tantalum platform based on the cavity design in Refs. [48,49]. Figure 2(a) presents a schematic diagram of the DFB cavity. In the active area, we form the DFB grating as corrugations in the height of the tantalum waveguide [Fig. 2(b), inset]. This takes advantage of the small optical power overlap with the tantalum waveguide structure ( $\approx 0.5\%$ ) to achieve a low grating feedback strength. A quarter-wave phase shift element is placed in the middle of the grating structure to facilitate a single lasing mode at the Bragg frequency of the grating [50]. Figure 2(b) presents the calculated etch-depth-dependent feedback strength as  $\kappa = (1/\Lambda)(\Delta n/\bar{n})$  with  $\Lambda = (\lambda_0/4)(1/n_0 + 1/n_1)$ ,  $\Delta n = |n_1 - n_0|$ , and  $\bar{n} = (n_0 + n_1)/2$  [50]. Here,  $\lambda_0$  is the feedback wavelength, and  $n_1$  and  $n_0$  are the effective modal indices of the grating segments with and without corrugation, respectively. We target a grating etch depth of 8 nm, corresponding to feedback strength of  $\kappa = 10 \text{ cm}^{-1}$  in a 1.2 mm long active area, resulting in cavities with  $\kappa L = 1.2$  and effective mirror reflectances of 29%.

We mount the laser chips on a temperature-controlled stage for optical testing and characterization at stage temperatures ranging from 6°C to 35°C. We sweep the injection current through the

diode while monitoring the voltage drop across the device and the output optical power of the laser. To monitor the output power, we butt-couple a wide-area photodiode to one facet of the chip and collect the generated light through 12°-angled facet couplers. The measured laser voltage (green) and optical power (purple) curves for a DFB laser with a grating period of 152 nm are plotted in Fig. 2(c) as a function of the injection current at 20°C stage temperature. The measured threshold current is 48 mA (threshold current density of 870 A/cm<sup>2</sup>) with a maximum recorded output power of 2 mW at 100 mA injection current. We estimate the per-facet slope efficiency of 0.05 W A<sup>-1</sup> (total slope efficiency of 0.1 W A<sup>-1</sup>). This can be improved to reach the values reported in Ref. [33] (0.43 W A<sup>-1</sup>) by optimizing the laser cavity design (i.e., DFB grating strength and length of the active region) and by reducing the optical propagation losses in the tantalum waveguides (currently limited by the unoptimized etch process and excess sidewall scattering). The kinks in the output power are attributed to heat-related longitudinal mode-hopping in the laser cavity [51]. The lasing mode is defined by the spectral alignment of the DFB grating resonance to one of the longitudinal modes of the cavity at a wavelength with high spectral gain. As the injection current is increased, the III–V gain spectra redshift at a higher rate than the DFB grating resonance. This results in the detuning of the cavity modes from the peak grating feedback, causing a drop in

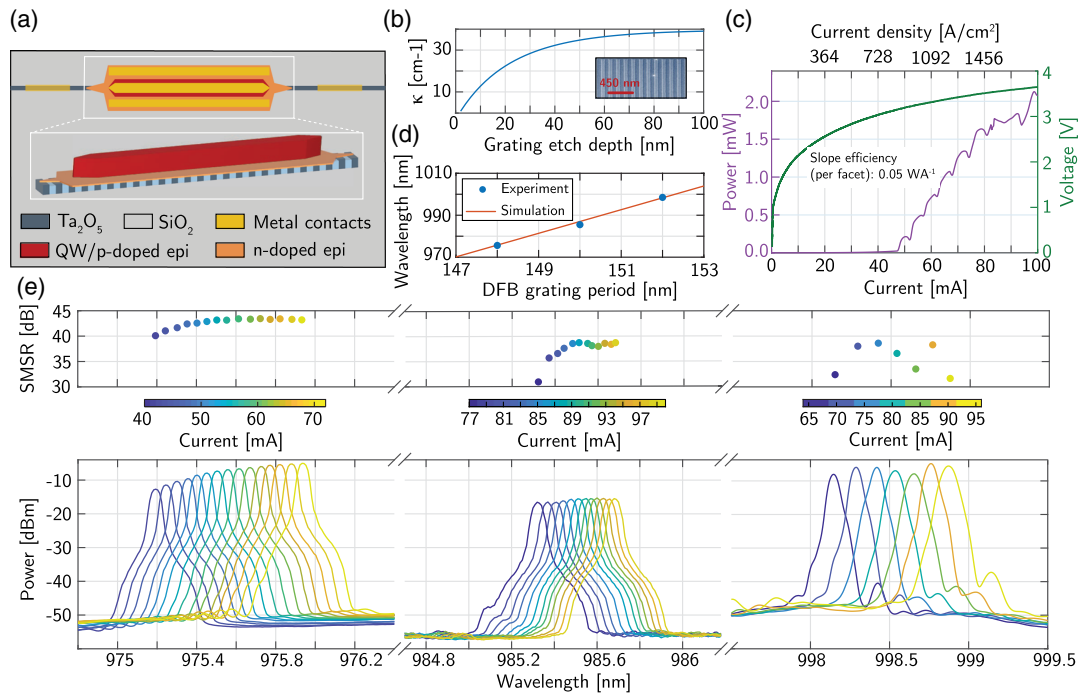


**Fig. 2.** Optical testing of the DFB lasers. (a) Schematic diagram of the DFB cavity with the low- $\kappa$  feedback gratings etched in the tantala waveguides. (b) Calculated DFB grating strength,  $\kappa$ , as a function of the tantala etch depth. (c) Measured laser power–current and voltage–current curves of a fabricated device operating at 998 nm. (d) Calculated and measured lasing wavelengths as a function of DFB grating period, showing excellent agreement within 1.5 nm. (e) Measured spectra and SMSR of lasers operating at 975 nm, 985 nm, and 998 nm, in left, center, and right panels, respectively.

the output power until eventually the next longitudinal mode is aligned. The observed voltage drop across the diode is larger than expected value of  $\approx 1.3$  V, as determined by the quantized energy levels in the QW. This higher voltage can be explained by the existence of sidewall recombination current in our devices. The etched sidewalls of the III–V laser mesa contain defects that, if not fully passivated, provide an electrical current path and cause nonradiative recombination of the carriers. As explained in Supplement 1, we can model the leakage current by assuming a diode ideality factor of larger than 2 in the standard PIN diode current–voltage model [50,52]. This extra sidewall recombination current and its mitigation through the development of effective sidewall passivation methods have been previously reported for micron-scale light-emitting diodes with dimensions similar to the laser structures reported in this work [53,54].

To measure the optical spectrum, we couple the laser output to a single-mode 980 nm lensed fiber ( $3 \text{ dB} \pm 1 \text{ dB}$  coupling efficiency) and record the spectrum with an optical spectrum analyzer (OSA) with a resolution bandwidth limit of 0.05 nm (15.6 GHz). Figure 2(e) presents the recorded spectra and side-mode suppression ratio (SMSR) of three DFB lasers with grating periods of 148 nm, 150 nm, and 152 nm on the left, center, and right panels, respectively. Phase heater elements on the two sides of the active region [Fig. 1(d)] enable a current-dependent, mode-hop free tuning range of  $>250$  GHz with tuning rates of 26.5 pm/mA, 16.6 pm/mA, and 24.0 pm/mA, respectively (refer to Supplement 1). Figure 2(d) presents the calculated and measured lasing wavelengths of the DFB lasers as a function of the feedback grating period. We observe excellent agreement between the designed and measured wavelengths within 1.5 nm. The lasing wavelength is calculated using  $\lambda = 2\bar{n}\Lambda$ . For accurate calculation of  $\bar{n}$ , we model the heat transfer in the semiconductor diode using

COMSOL multiphysics to simulate the QW device temperature at a certain injection current. We then estimate  $n_0$  and  $n_1$  at the simulated device temperature using the refractive index data for tantala [36] and the III–V material stack [55].

To better understand the single-mode operation of the lasers, we plot a two-dimensional map of the DFB peak lasing wavelength and SMSR for a laser operating at 985 nm as a function of injection current (horizontal axis) and stage temperatures (vertical axis) in Figs. 3(a) and 3(b), respectively. To identify the single-mode operation region, we adjust the stage temperature from 6°C to 32°C in 1°C increments, ensuring stability at each setpoint with a tolerance of  $\pm 5$  m°C. At each temperature setpoint, the injection current is swept from 0 mA to 100 mA in 1 mA increments, and the optical spectrum is recorded using an OSA. The white areas in Figs. 3(a) and 3(b) depict the current and temperature settings at which the laser is operating sub-threshold. A redshift in the peak lasing wavelength is visible in Fig. 3(a) as a function of increasing injection current and stage temperature. We observe a longitudinal mode-hop in the lasing wavelength at injection currents around 65–75 mA, depending on the stage temperature. At currents below this level, the DFB laser has a multi-mode behavior as evidenced by the low SMSR. After the mode-hopping, the laser operates in a single-mode region where the SMSR stays  $>30$  dB for a wide range of injection currents (70 mA to 100 mA) and stage temperatures (6°C to 28°C).

We measure the power spectral density (PSD) of the laser frequency noise (FN) using a fiber-based, calibrated, unbalanced Mach–Zehnder interferometer (MZI). The MZI has a free spectral range of 800 MHz and acts as an optical frequency discriminator. Figure 3(c) presents the measured FN PSD at an injection current of 76 mA for a DFB laser operating at 976 nm with 43 dB SMSR. At Fourier frequency offsets of  $<1$  MHz, the FN PSD scales

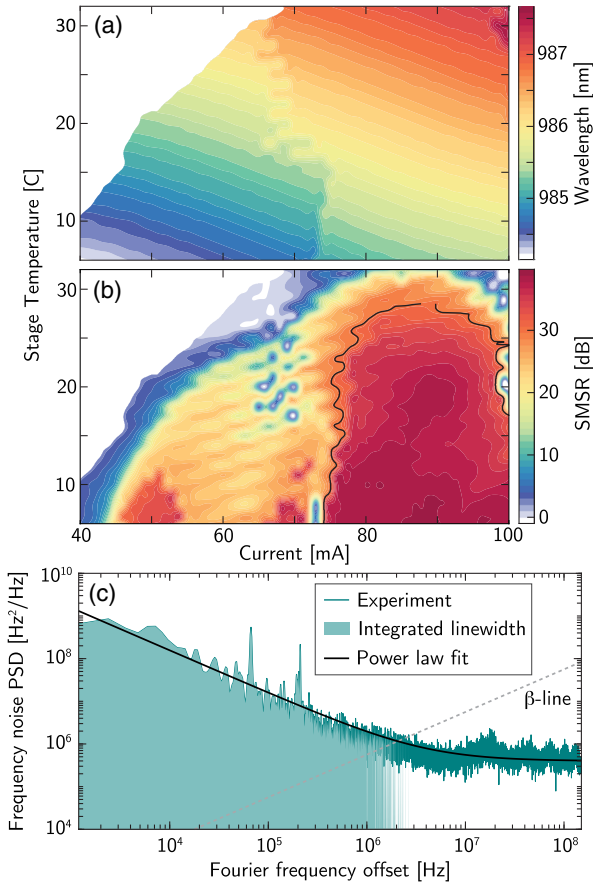


**Fig. 3.** Single-mode operation and frequency noise characterization of DFB lasers. Two-dimensional mapping of the (a) lasing wavelength and (b) side-mode suppression ratio as a function of increasing stage temperature and injection current for a laser with a feedback grating period of 150 nm. (c) Frequency noise power spectral density of a laser operating at 976 nm (feedback grating period 148 nm and injection current 76 mA).

inversely with the frequency as expected for a DFB laser. The FN PSD flattens at the white noise level of  $4 \times 10^5 \text{ Hz}^2/\text{Hz}$ , indicating a laser fundamental linewidth of 1.2 MHz, limited by the cavity length [56]. We calculate the integrated linewidth of the laser based on two methods, namely the  $1/\pi$  [57] and the  $\beta$ -separation line [58]. In the  $1/\pi$  method, the integrated linewidth is defined as the Fourier frequency offset at which the accumulated phase noise, i.e., the area under the FN PSD curve, reaches  $1/\pi \text{ rad}^2$ . For the data in Fig. 3(c), we calculate the accumulated phase noise starting from the highest frequency offset of the measurement (150 MHz), resulting in an integrated linewidth of 2.0 MHz. When applied to an ideal laser source with white frequency noise, the  $1/\pi$  method results in the full-width half-maximum of the Lorentzian lineshape [59]. The  $\beta$ -line method gives a better estimate of the integrated linewidth for laser sources with added frequency noise other than the white noise since it also accounts for technical and flicker noise. In this method, the frequency noise spectrum is divided into two regions separated by the  $\beta$ -separation line  $S_{\delta\nu} = 8 \ln(2) f / \pi^2$  [dashed line in Fig. 3(c)]. Here,  $S_{\delta\nu}$  is the FN PSD, and  $f$  is the Fourier frequency offsets. In the FN PSD region with  $S_{\delta\nu} < \beta$ -line, the noise frequency is too fast, and its modulation index is too slow to cause a significant broadening to the laser linewidth. Conversely, in the region with  $S_{\delta\nu} > \beta$ -line [highlighted with green in Fig. 3(c)], the noise level is high compared to the Fourier

frequency, and it causes a Gaussian broadening of the laser lineshape. In this method, the integrated laser linewidth is calculated as the area under the FN PSD curve in the high modulation index region. We calculate the integrated linewidth of 9.4 MHz using the  $\beta$ -separation line method.

#### 4. SYSTEM-LEVEL OPERATION AND OUTLOOK

Figure 4(a) presents a three-dimensional schematic of a heterogeneous III-V/tantala PIC, highlighting the versatile integration of passive and active components with different functionalities. In addition to single-mode lasers [Fig. 4(b)], we demonstrate a variety of photonic components. The low optical loss in the deposited tantala layer, along with the  $\text{SiO}_2$  top-cladding, enables fabrication of high-quality factor (high-Q) microring resonators [37]. These resonators are essential for applications requiring high-performance cavities, such as narrow-band filters and efficient nonlinear optical processes. Figure 4(c) presents a high-Q microring with an intrinsic quality factor of  $2.5 \times 10^6$  at 1064 nm, fabricated with a ring width of 2.0  $\mu\text{m}$ . Figure 4(d) demonstrates a 1.5 mm long FP laser with a 45 mA threshold current ( $430 \text{ A}/\text{cm}^2$  threshold current density) and  $> 2 \text{ mW}$  waveguide-coupled output power. SOAs are an integral part of photonic systems. Figure 4(e) presents the on-chip gain spectrum of a 2 mm long integrated SOA operating at 105 mA injection current. Such devices are often used to enable system functionality in applications requiring high optical power, such as nonlinear optical interactions for frequency comb generation and wavelength conversion in microring resonators. Here, the scattered data points are measured using a tunable laser coupled to the TE<sub>0</sub> mode of the SOAs with an on-chip input power of 25  $\mu\text{W}$ . The black curve represents the fit to the data using  $G(\lambda) = G_p \exp[-A(\lambda - \lambda_p)^2]$ , where  $G_p$  is the peak on-chip gain,  $\lambda_p$  is the peak gain wavelength, and  $A$  is related to the 3 dB gain bandwidth by  $\Delta\lambda = 2\sqrt{\ln 2/A}$  [60]. We calculate the peak gain, wavelength, and 3 dB bandwidth of 24.5 dB, 987.4 nm, and 8.5 nm, respectively. We also calculate the peak modal gain,  $g_{\text{net}}(\lambda_p)$ , of  $28.2 \text{ cm}^{-1}$  from the  $G_p$  factor using  $G_p = \exp[g_{\text{net}}(\lambda_p)L]$  [60]. The reported peak gain offers a  $\approx 2.5 \text{ dB}$  improvement over the previously reported state-of-the-art value measured in heterogeneous  $\text{Si}_3\text{N}_4$  PICs [33]. The design of the gain region in the SOAs is identical to that of the laser devices (i.e., a constant III-V ridge width of 5  $\mu\text{m}$ ). It is, however, possible to design tapered amplifiers by tapering the width of the III-V mesa. The confinement factor of the optical mode in the two QWs is dictated by the large effective index contrast between the tantala and III-V structures. One can benefit from this to achieve high confinement for a large range of III-V widths and to design tapered amplifiers. Efficient operation of such devices, however, will be limited by their extensive heat generation. Currently, heterogeneous PICs rely on heat dissipation through the backside Si substrate, which is insufficient for the operation of high-power devices. Alternatively, methods such as flip-chip bonding of the PIC chip to an AlN sub-mount should be considered to enable efficient heat transfer and high-power operation.

Emerging quantum integrated photonic systems require on-chip lasers operating in the visible spectrum, extending down to ultraviolet wavelengths. Targeted wavelength conversion of a common pump laser through nonlinear optical interactions, such as OPO [38,61–63] and second harmonic generation [64],

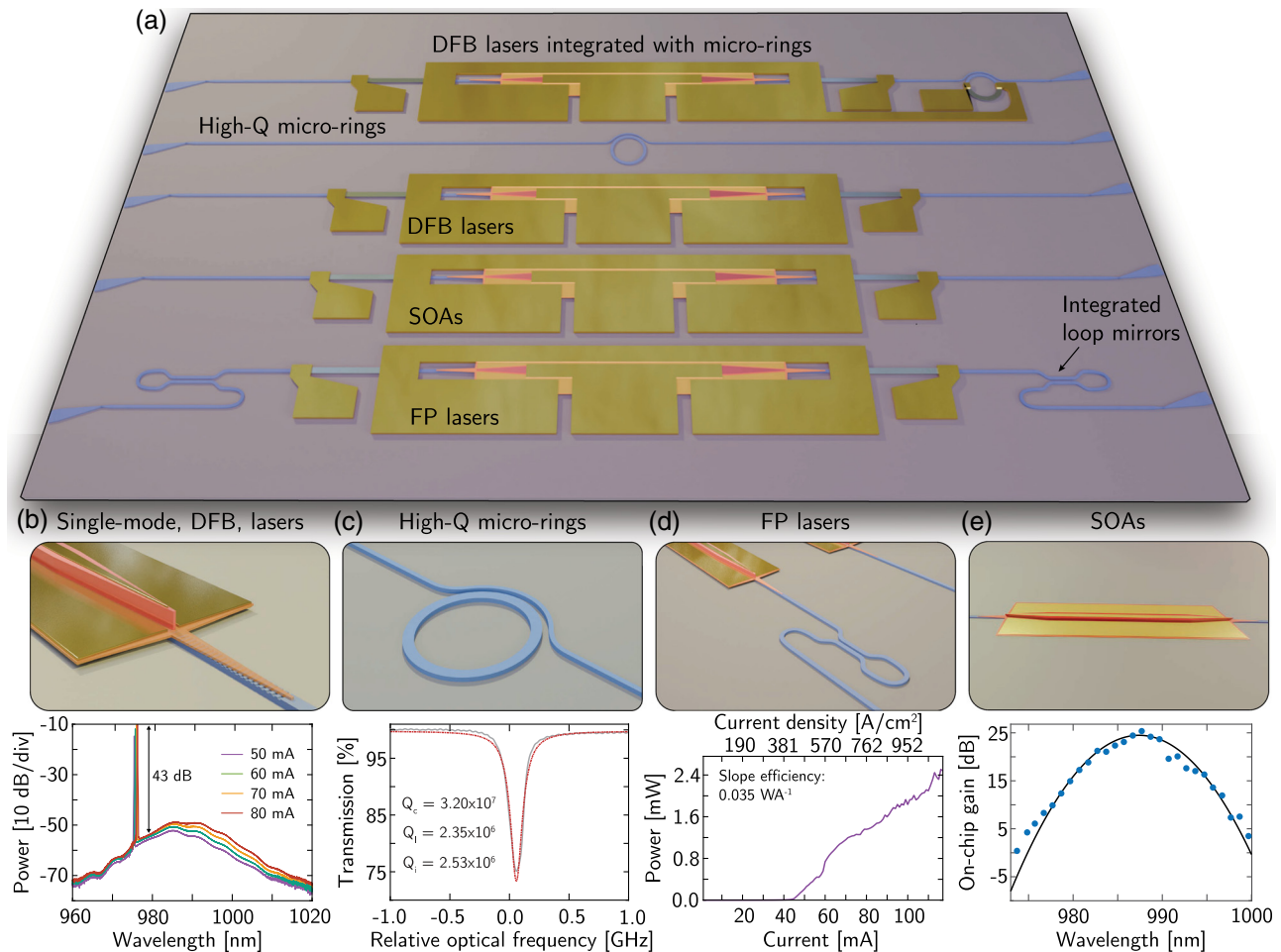


**Fig. 4.** (a) Three-dimensional rendering of the fabricated heterogeneous tantalum PIC supporting versatile, wafer-scale, integration of active components with low-loss passive PICs. (b–e) Active and passive functionalities are demonstrated on the platform. From left to right: (b) single-mode lasers based on distributed feedback cavities, (c) ultra-low-loss passive tantalum waveguides and high-quality-factor microring resonators, (d) Fabry–Pérot (FP) lasers with integrated loop mirrors etched in the tantalum waveguides, and (e) tantalum-integrated SOA with 24.5 dB small signal gain at 987.4 nm.

is shown to be a viable path for on-chip generation of short, hard-to-access wavelengths, specifically within the “green gap” [61,65] and blue colors [64]. We test the utility of integrated DFB lasers for such nonlinear optical interactions by pumping OPO processes in microring resonators fabricated in a separate tantalum PIC. Figure 5(a) presents the experimental setup for OPO pumping. We couple the laser output [operating at 976 nm, Fig. 2(e), left panel] into a 980 nm single-mode fiber. We then use a fiber-coupled optical amplifier to amplify the laser light to  $> 100 \text{ mW}$ , required to reach the OPO process threshold. The amplified light is then edge-coupled into a separate tantalum PIC with the fabricated microring resonators using lensed fibers with 6 dB coupling loss. For OPO pumping, we current- and temperature-tune the laser wavelength into resonance with the TE<sub>0</sub> optical mode of the microring resonators and monitor the output optical spectra with an OSA [Fig. 5(b)].

The microrings of different widths provide phase-matching conditions to generate signal and idler lights at different wavelengths. Figure 5(c) compares the measured signal and idler wavelengths (scattered data points) with theoretical designs (dashed lines) for different ring widths. We design the OPO process in microring resonators by following the method outlined in [38,61] for geometrical group-velocity dispersion (GVD) engineering of the resonator waveguides. The resonator GVD can be

controlled by tailoring the waveguide thickness and width and the resonator radius. This enables control of the OPO phase-matching condition through geometrical tuning of the effective modal index of the pump, signal, and idler waves. To emphasize platform compatibility for future heterogeneous integration of lasers and OPO resonators, we design microring geometries in a tantalum layer with a similar thickness used for laser integration (570 nm). The further choice of resonator radius of  $45 \mu\text{m}$  and resonator waveguide widths in the range of 930–970 nm facilitates normal GVD values at the pump wavelength of 976 nm, which is required to realize wide-span OPO processes [61]. Increasing the microring width results in the generation of wider-span OPO spectra and enables short-wavelength signal generation. As presented with orange and red curves in Fig. 5(b), we record generated signal wavelengths of 778 nm and 750 nm at the output of microrings with widths of 959 nm and 966 nm, respectively. The generated signal at 778 nm is suitable for integration with emerging portable atomic clocks based on two-photon absorption in Rb-87 atomic vapor cells [66].

The OPO pumping setup in Fig. 5(a) includes two isolators to prevent back-reflections into the integrated DFB laser cavity. Heterogeneous photonic integrated circuits suffer from the lack of reliable on-chip isolators with optical power-independent high isolation ratio ( $> 30 \text{ dB}$ ). Alternatively, in an integrated laser+OPO

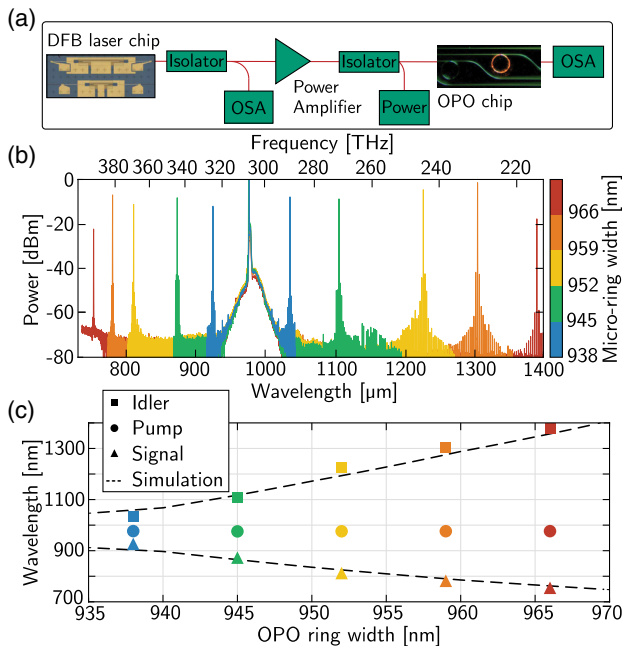


**Fig. 5.** OPO pumped with the integrated DFB laser. (a) DFB laser output is coupled into a single-mode fiber and amplified to 100 mW level before being coupled to a second tantala chip with the high-quality-factor (high-Q) rings. Fiber-coupled optical isolators are used to prevent back-reflections from entering the laser cavity. The output spectra of the high-Q resonators are monitored with an OSA. (b) Measured output OPO spectra of the microring resonators with different ring widths. (c) Simulated (dashed line) and measured (scattered dots) wavelengths of the generated signal and idler colors as a function of microring widths for the DFB pump wavelength of 976 nm. The data points are colored to match their corresponding OSA spectra in part (b).

system [depicted in Fig. 4(a), top device], the back-reflections from the microring can be engineered for linewidth narrowing of the pump laser through self-injection locking [67]. This would be possible by utilizing a phase heater element on the bus waveguide connecting the laser output to the microresonator. Such a heater element can be utilized to tune the phase of the back-reflected waves to achieve self-injection locking [46] and enable isolator-free photonic circuits [68].

## 5. CONCLUSION

Ultra-low material loss and advanced fabrication processes have established tantala as a prime material platform for a variety of on-chip linear and nonlinear photonic applications, including dielectric metasurface photonics [69], frequency comb generation [37,70], supercontinuum generation [37,71], and wide-span OPO [62,63]. Here, we introduce active functionalities on tantala PICs through heterogeneous integration with InGaAs-on-GaAs QW gain material. The integration method introduced here enables high-yield, wafer-scale, co-fabrication of passive and active components with >95% surface area yield on a 76.2 mm wafer. Integration of III-V gain sections with passive waveguides and external cavities enables the demonstration of FP lasers, SOAs with >21 dB gain, and current-tunable DFB lasers operating at 980 nm wavelength band with 43 dB side-mode suppression ratio and single-mode tuning range wider than  $4\times$  the longitudinal mode spacing of 60 GHz.

We utilized our DFB laser as a pump source for  $\chi^{(3)}$  microring resonator-based degenerate OPO to demonstrate the system-level functionality and utility of the on-chip active components. The resonators were designed and fabricated on the same 570 nm thick tantala platform used for the laser integration to show the potential for future integration of pump laser diodes with microring resonators for monolithic OPOs. Our widest signal-to-idler frequency span is 183 THz, and the shortest wavelength signal generated is at 752 nm, limited by the available resonator geometries.

The heterogeneous integration presented in this work is agnostic to the design of the GaAs-based QW layer stack. We can take advantage of such versatility to realize photonic integrated circuits with active functionalities at shorter wavelengths down to  $\approx 700$  nm. Utilizing this platform, one can envision a heterogeneous PIC with active components operating in the 700–980 nm wavelength range. In such a platform, pump lasers would be integrated with a variety of passive components designed for different nonlinear optical interactions, such as frequency comb generation and nonlinear wavelength conversion to shorter, hard-to-access, wavelengths. Fully functional photonic systems can be designed to support the generation, routing, and manipulation of multiple wavelengths needed for the operation of quantum systems based on specific atomic vapor cells or trapped ions. Such integrated quantum technologies have the potential to reshape a variety of high-impact industries through scalable miniaturization. As such, the deployment of these systems can mark a paradigm shift by offering robust, portable, and potentially autonomous (GPS-free) PNT systems.

**Funding.** National Institute of Standards and Technology (NIST-on-a-chip); Defense Advanced Research Projects Agency (LUMOS); National Science Foundation (OMA-2016244); Air Force Office of Scientific Research (FA9550-20-1-0004 Project Number 19RT1019).

**Acknowledgment.** We thank Jeffrey Shainline, Scott Diddams, John Kitching, Kartik Srinivasan, and David Carlson for useful discussions and inputs on the manuscript. Product disclaimer: Any mention of commercial products is for information only; it does not imply recommendation or endorsement by NIST.

**Disclosures.** The authors declare no competing interests. Eric J. Stanton is the co-founder of EMode Photonix.

**Data availability.** Data underlying the results presented in this paper are not publicly available at this time but may be obtained from the authors upon reasonable request.

**Supplemental document.** See Supplement 1 for supporting content.

## REFERENCES

1. C. D. Bruzewicz, J. Chiaverini, R. McConnell, *et al.*, “Trapped-ion quantum computing: progress and challenges,” *Appl. Phys. Rev.* **6**, 021314 (2019).
2. I. Pogorelov, T. Feldker, C. D. Marciniak, *et al.*, “Compact ion-trap quantum computing demonstrator,” *PRX Quantum* **2**, 020343 (2021).
3. N. Poli, C. W. Oates, P. Gill, *et al.*, “Optical atomic clocks,” *La Rivista del Nuovo Cimento* **36**, 555–624 (2013).
4. A. D. Ludlow, M. M. Boyd, J. Ye, *et al.*, “Optical atomic clocks,” *Rev. Mod. Phys.* **87**, 637–701 (2015).
5. W. F. McGrew, X. Zhang, H. Leopardi, *et al.*, “Towards the optical second: verifying optical clocks at the SI limit,” *Optica* **6**, 448–454 (2019).
6. B. Canuel, F. Leduc, D. Holleville, *et al.*, “Six-axis inertial sensor using cold-atom interferometry,” *Phys. Rev. Lett.* **97**, 010402 (2006).
7. Y.-J. Chen, A. Hansen, G. W. Hoth, *et al.*, “Single-source multiaxis cold-atom interferometer in a centimeter-scale cell,” *Phys. Rev. Appl.* **12**, 014019 (2019).

8. J. Lee, R. Ding, J. Christensen, *et al.*, “A compact cold-atom interferometer with a high data-rate grating magneto-optical trap and a photonics-integrated-circuit-compatible laser system,” *Nat. Commun.* **13**, 5131 (2022).
9. D. Budker and M. Romalis, “Optical magnetometry,” *Nat. Phys.* **3**, 227–234 (2007).
10. V. Shah, S. Knappe, P. D. D. Schwindt, *et al.*, “Subpicotesla atomic magnetometry with a microfabricated vapour cell,” *Nat. Photonics* **1**, 649–652 (2007).
11. G. Rosi, F. Sorrentino, L. Cacciapuoti, *et al.*, “Precision measurement of the Newtonian gravitational constant using cold atoms,” *Nature* **510**, 518–521 (2014).
12. L.-A. Liew, S. Knappe, J. Moreland, *et al.*, “Microfabricated alkali atom vapor cells,” *Appl. Phys. Lett.* **84**, 2694–2696 (2004).
13. J. M. Pate, J. Kitching, and M. T. Hummon, “Microfabricated strontium atomic vapor cells,” *Opt. Lett.* **48**, 383–386 (2023).
14. S. Seidelin, J. Chiaverini, R. Reichle, *et al.*, “Microfabricated surface-electrode ion trap for scalable quantum information processing,” *Phys. Rev. Lett.* **96**, 253003 (2006).
15. M. T. Hummon, S. Kang, D. G. Bopp, *et al.*, “Photonics chip for laser stabilization to an atomic vapor with 10–11 instability,” *Optica* **5**, 443–449 (2018).
16. Z. L. Newman, V. Maurice, T. Drake, *et al.*, “Architecture for the photonics integration of an optical atomic clock,” *Optica* **6**, 680–685 (2019).
17. R. J. Niffenegger, J. Stuart, C. Sorace-Agaskar, *et al.*, “Integrated multi-wavelength control of an ion qubit,” *Nature* **586**, 538–542 (2020).
18. K. K. Mehta, C. Zhang, M. Malinowski, *et al.*, “Integrated optical multi-ion quantum logic,” *Nature* **586**, 533–537 (2020).
19. A. Isichenko, N. Chauhan, D. Bose, *et al.*, “Photonics integrated beam delivery for a rubidium 3D magneto-optical trap,” *Nat. Commun.* **14**, 3080 (2023).
20. A. Kodigala, M. Gehl, G. W. Hoth, *et al.*, “High-performance silicon photonics single-sideband modulators for cold-atom interferometry,” *Sci. Adv.* **10**, eade4454 (2024).
21. T. F. Gallagher, *Rydberg Atoms, Cambridge Monographs on Atomic, Molecular and Chemical Physics* (Cambridge University Press, 1994).
22. N. Schlossberger, N. Prajapati, S. Berweger, *et al.*, “Rydberg states of alkali atoms in atomic vapour as SI-traceable field probes and communications receivers,” *Nat. Rev. Phys.* **6**, 606–620 (2024).
23. I. V. Inlek, “Multi-species trapped atomic ion modules for quantum networks,” Ph.D. thesis (University of Maryland, 2016).
24. G. Imreh, “Implementing segmented ion trap designs for quantum computing,” Ph.D. thesis (University of Oxford, 2008).
25. M. Brownnutt, “<sup>88</sup>Sr<sup>+</sup> ion trapping techniques and technologies for quantum information processing,” Ph.D. thesis (Imperial College London, 2007).
26. H. Ball, C. D. Marciniak, R. N. Wolf, *et al.*, “Site-resolved imaging of beryllium ion crystals in a high-optical-access Penning trap with inbore optomechanics,” *Rev. Sci. Instrum.* **90**, 053103 (2019).
27. T. Komljenovic, D. Huang, P. Pintus, *et al.*, “Photonics integrated circuits using heterogeneous integration on silicon,” *Proc. IEEE* **106**, 2246–2257 (2018).
28. C. Xiang and J. E. Bowers, “Integrated lasers for data center silicon photonics-integrated circuits,” in *Integrated Photonics for Data Communication Applications*, M. Glick, L. Liao, and K. Schmidtke, eds. (Elsevier, 2023), Integrated Photonics Apps Specific Design & Manufacturing, pp. 35–68.
29. J. E. Bowers, “A tutorial on silicon heterogeneous integrated photonics integrated circuits: from data centers to sensors,” in *2023 IEEE Photonics Conference (IPC)* (2023), pp. 1–2.
30. S. Shekhar, W. Bogaerts, L. Chrostowski, *et al.*, “Roadmapping the next generation of silicon photonics,” *Nat. Commun.* **15**, 751 (2024).
31. C. Shang, Y. Wan, J. Selvidge, *et al.*, “Perspectives on advances in quantum dot lasers and integration with Si photonics integrated circuits,” *ACS Photonics* **8**, 2555–2566 (2021).
32. A. W. Fang, H. Park, O. Cohen, *et al.*, “Electrically pumped hybrid AlGaInAs-silicon evanescent laser,” *Opt. Express* **14**, 9203–9210 (2006).
33. M. A. Tran, C. Zhang, T. J. Morin, *et al.*, “Extending the spectrum of fully integrated photonics to submicrometre wavelengths,” *Nature* **610**, 54–60 (2022).
34. Z. Zhang, B. Shen, M. A. Tran, *et al.*, “Photonics integration platform for rubidium sensors and beyond,” *Optica* **10**, 752–753 (2023).
35. T. J. Morin, J. Peters, M. Li, *et al.*, “Coprocessed heterogeneous near-infrared lasers on thin-film lithium niobate,” *Opt. Lett.* **49**, 1197–1200 (2024).
36. J. A. Black, R. Streater, K. F. Lamee, *et al.*, “Group-velocity-dispersion engineering of tantalum integrated photonics,” *Opt. Lett.* **46**, 817–820 (2021).
37. H. Jung, S.-P. Yu, D. R. Carlson, *et al.*, “Tantalum Kerr nonlinear integrated photonics,” *Optica* **8**, 811–817 (2021).
38. X. Lu, G. Moille, A. Singh, *et al.*, “Milliwatt-threshold visible-telecom optical parametric oscillation using silicon nanophotonics,” *Optica* **6**, 1535–1541 (2019).
39. G. Roelkens, J. Zhang, L. Bogaert, *et al.*, “Present and future of micro-transfer printing for heterogeneous photonics integrated circuits,” *APL Photonics* **9**, 010901 (2024).
40. J. Zhang, G. Muliuk, J. Juvert, *et al.*, “III-V-on-Si photonics integrated circuits realized using micro-transfer-printing,” *APL Photonics* **4**, 110803 (2019).
41. M. Tran, Z. Zhang, B. Shen, *et al.*, “Heterogeneous photonics in visible and beyond,” in *CLEO 2024* (Optica Publishing Group, 2024), p. AW3J.3.
42. A. E. Dorche, N. Nader, E. J. Stanton, *et al.*, “Heterogeneously integrated near-infrared DFB laser on tantalum pentoxide,” in *Optical Fiber Communication Conference (OFC) 2023* (Optica Publishing Group, 2023), p. Tu3C.6.
43. A. E. Dorche, N. Nader, E. J. Stanton, *et al.*, “Heterogeneously integrated InGaAs DFB laser on tantalum pentoxide,” in *CLEO 2023* (Optica Publishing Group, 2023), p. SM2J.5.
44. X. Lu, L. Chang, M. A. Tran, *et al.*, “Emerging integrated laser technologies in the visible and short near-infrared regimes,” *Nat. Photonics* **18**, 1010–1023 (2024).
45. J. Ling, J. Staffa, H. Wang, *et al.*, “Self-injection locked frequency conversion laser,” *Laser Photonics Rev.* **17**, 2200663 (2023).
46. C. Xiang, J. Liu, J. Guo, *et al.*, “Laser soliton microcombs heterogeneously integrated on silicon,” *Science* **373**, 99–103 (2021).
47. B. Li, W. Jin, L. Wu, *et al.*, “Reaching fiber-laser coherence in integrated photonics,” *Opt. Lett.* **46**, 5201–5204 (2021).
48. A. W. Fang, E. Lively, Y.-H. Kuo, *et al.*, “A distributed feedback silicon evanescent laser,” *Opt. Express* **16**, 4413–4419 (2008).
49. S. Srinivasan, A. W. Fang, D. Liang, *et al.*, “Design of phase-shifted hybrid silicon distributed feedback lasers,” *Opt. Express* **19**, 9255–9261 (2011).
50. L. A. Coldren, S. W. Corzine, and M. L. Mashanovitch, *Diode Lasers and Photonic Integrated Circuits* (John Wiley & Sons, Incorporated, 2012).
51. D. Huang, M. A. Tran, J. Guo, *et al.*, “High-power sub-kHz linewidth lasers fully integrated on silicon,” *Optica* **6**, 745–752 (2019).
52. G. P. Agrawal and N. K. Dutta, *Semiconductor Lasers* (Springer New York, 1993).
53. M. S. Wong, J. A. Kearns, C. Lee, *et al.*, “Improved performance of AlGaInP red micro-light-emitting diodes with sidewall treatments,” *Opt. Express* **28**, 5787–5793 (2020).
54. P.-W. Chen, P.-W. Hsiao, H.-J. Chen, *et al.*, “On the mechanism of carrier recombination in downsized blue micro-LEDs,” *Sci. Rep.* **11**, 22788 (2021).
55. S. Gehrsitz, F. K. Reinhart, C. Gourgon, *et al.*, “The refractive index of Al<sub>x</sub>Ga<sub>1-x</sub>As below the band gap: Accurate determination and empirical modeling,” *J. Appl. Phys.* **87**, 7825–7837 (2000).
56. C. Henry, “Phase noise in semiconductor lasers,” *J. Lightwave Technol.* **4**, 298–311 (1986).
57. D. Hjelme, A. Mickelson, and R. Beausoleil, “Semiconductor laser stabilization by external optical feedback,” *IEEE J. Quantum Electron.* **27**, 352–372 (1991).
58. G. D. Domenico, S. Schilt, and P. Thomann, “Simple approach to the relation between laser frequency noise and laser line shape,” *Appl. Opt.* **49**, 4801–4807 (2010).
59. W. Liang, V. S. Ilchenko, D. Eliyahu, *et al.*, “Ultralow noise miniature external cavity semiconductor laser,” *Nat. Commun.* **6**, 7371 (2015).
60. N. Volet, A. Spott, E. J. Stanton, *et al.*, “Semiconductor optical amplifiers at wavelength on silicon,” *Laser Photonics Rev.* **11**, 1600165 (2017).
61. X. Lu, G. Moille, A. Rao, *et al.*, “On-chip optical parametric oscillation into the visible: generating red, orange, yellow, and green from a near-infrared pump,” *Optica* **7**, 1417–1425 (2020).
62. J. A. Black, G. Brodnik, H. Liu, *et al.*, “Optical-parametric oscillation in photonics-crystal ring resonators,” *Optica* **9**, 1183–1189 (2022).

63. G. M. Brodnik, H. Liu, D. R. Carlson, *et al.*, “Nanophotonics oscillators for laser conversion beyond an octave,” (2024).
64. T. Park, H. S. Stokowski, V. Ansari, *et al.*, “High-efficiency second harmonic generation of blue light on thin-film lithium niobate,” *Opt. Lett.* **47**, 2706–2709 (2022).
65. Y. Sun, J. Stone, X. Lu, *et al.*, “Advancing on-chip Kerr optical parametric oscillation towards coherent applications covering the green gap,” *Light Sci. Appl.* **13**, 201 (2024).
66. V. Maurice, Z. L. Newman, S. Dickerson, *et al.*, “Miniaturized optical frequency reference for next-generation portable optical clocks,” *Opt. Express* **28**, 24708–24720 (2020).
67. T. C. Briles, J. R. Stone, S. B. Papp, *et al.*, “Generation of octave-spanning microresonator solitons with a self injection-locked DFB laser,” in *2019 IEEE Avionics and Vehicle Fiber-Optics and Photonics Conference (AVFOP)* (2019), pp. 1–2.
68. C. Xiang, W. Jin, O. Terra, *et al.*, “3D integration enables ultralow-noise isolator-free lasers in silicon photonics,” *Nature* **620**, 78–85 (2023).
69. C. Zhang, L. Chen, Z. Lin, *et al.*, “Tantalum pentoxide: a new material platform for high-performance dielectric metasurface optics in the ultraviolet and visible region,” *Light Sci. Appl.* **13**, 23 (2024).
70. G. Spektor, J. Zang, A. Dan, *et al.*, “Photonics bandgap microcombs at 1064 nm,” *APL Photonics* **9**, 021303 (2024).
71. K. F. Lamee, D. R. Carlson, Z. L. Newman, *et al.*, “Nanophotonics tantala waveguides for supercontinuum generation pumped at 1560 nm,” *Opt. Lett.* **45**, 4192–4195 (2020).